Design methodology for high-speed synchronous reluctance machines

Cristian Babetto[1], Giacomo Bacco[1], Nicola Bianchi[1] ✉

[1]Department of Industrial Engineering, University of Padova, Padova 35131, Italy
✉ E-mail: nicola.bianchi@unipd.it

Abstract: This study presents two design methodologies for high-speed synchronous reluctance (REL) machines. The interest for high-speed drives comes from the request for compactness and high efficiency. The synchronous REL motors have been widely studied for several applications, but a coherent design procedure for high speed has not been proposed in the literature. The study proposes some analytical procedures to get an initial design. Then the rotor geometry optimisation through a differential evolution algorithm is described. Finally, a design example is given and thoroughly analysed using these two approaches.

1 Introduction

The current-controlled synchronous reluctance (REL) motor is well known for its cheap rotor structure and good performance. The electromagnetic and mechanical features of this machine have been highlighted in the literature where it is proposed as a valid alternative to both permanent magnet and induction machines in many applications [1–5]. As a consequence, the REL motor has been used in several applications, including home appliance, pump and ventilation systems, traction, operating tools, and so on [6, 7].

The REL rotor is characterised by an intrinsic fault-tolerant capability since there is no back electromotive force without supply and then no short-circuit current [8] or braking torque in the case of fault [9]. The drawbacks of the synchronous REL machine are the low power factor, in comparison to other synchronous machines, and the complex rotor design required for the torque ripple minimisation. To increase the power factor, the rotor anisotropy (i.e. the ratio between the d-axis and q-axis inductance) has to be necessarily high [10–13]. This aspect is achieved with a rotor structure formed by several air flux barriers, whose number is usually two or more [14]. The torque ripple, which characterises the torque waveform [1], is due to the interaction between the stator space harmonics and the rotor anisotropy. Rotor skewing is often not enough to reduce the ripple; so, a proper choice of the

position of the flux-barrier ends is mandatory, and some solutions have been described in [15–18].

The REL motor has not been deeply studied for high-speed applications [19], where permanent magnet machines are mainly considered [20–23]. Therefore, this paper describes a guideline to properly design the synchronous REL machine suitable for high-speed applications. The main target is to give some guidelines for an accurate design of the rotor geometry to obtain a robust mechanical structure, a quite high torque density, and a low torque ripple. A particular care is paid to the rotor rib thicknesses, designed to guarantee the structural integrity of the rotor [24], and to minimise the q-axis magnetic flux. In fact, the thickness of these iron ribs has to be wide enough to mechanically sustain the rotor and it increases as the design speed increases [25].

At first, an analytical model is adopted [26] to derive a preliminary geometry. The stator geometry is fixed and the focus is on the rotor geometry. The effect of the iron ribs and their influence on the increase in the q-axis flux is taken into account. The flux-barrier end angles are selected so as to minimise the torque oscillation [4, 16, 18, 26]. Then, the purpose is to maximise the average electromagnetic torque, according to a fixed speed. This is done through adjusting the quantity of air present in the rotor.

Second, a finite element (FE) analysis is carried out to validate the results obtained by means of the analytical approach. Then, an optimisation is employed to optimise the position of the flux-barrier in the rotor, with the purpose of reducing the q-axis flux through the iron bridges (which causes the decrease in rotor anisotropy and average torque), and the torque ripple. The Pareto front is reported highlighting the potentials and the drawback of the optimal solutions. Finally, a thorough analysis of one optimal solution has been performed. It includes a full electromagnetic analysis to determine also accurate iron losses and a mechanical analysis under centrifugal stress to determine local stresses on the rotor and to verify the integrity of the structure (Fig. 1).

2 Analytical approach

2.1 Choice of flux-barrier angles

The analytical model presented hereafter [18] is used to determine the flux-barrier geometry of an REL motor. The assumptions considered are:

i. to neglect the saturation of the ferromagnetic material,
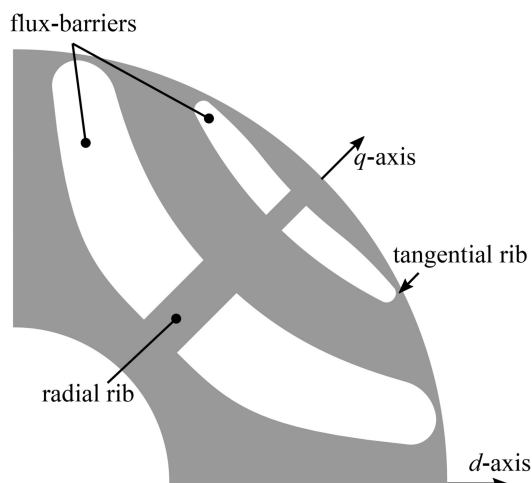ii. to neglect the stator slotting effect,

Fig. 1 *Example of one rotor pole of a synchronous REL machine with two flux barriers per pole*

iii. to neglect the rotor iron ribs, and
iv. to consider rotor magnetic scalar potentials constants and with constant steps.

Through this model, it is possible to predict the combinations of flux-barrier angles which lead to the lower torque ripples.

2.1.1 One flux-barrier rotor: Torque harmonics are produced by a couple of electric loading harmonics. In fact, the torque ripple of order h is due to the electric loading harmonics $\nu_1 = (1 - h)$ and $\nu_2 = (1 + h)$, where $h = 6n, n \in \mathbb{N}$.

The hypothesis of constant current angle, $\alpha_i^e = 45°$, is considered throughout the following derivation as it represents the worst-case scenario in practical applications ($\alpha_i^e \geq 45°$). Then, the torque ripple expression for the two harmonics becomes [18]

$$\left[\Delta \tau_{\mathrm{m}}^{(h)}\right]^2 \propto \left|\frac{\sin \nu_1 \vartheta_{\mathrm{b}}^{\mathrm{e}}}{\nu_1}\right|^2 + \left|\frac{\sin \nu_2 \vartheta_{\mathrm{b}}^{\mathrm{e}}}{\nu_2}\right|^2 \quad (1)$$

Imposing to zero the derivative of the torque ripple with respect to $\vartheta_{\mathrm{b}}^{\mathrm{e}}$, it results

$$\nu_2 \sin(2\nu_1 \vartheta_{\mathrm{b}}^{\mathrm{e}}) + \nu_1 \sin(2\nu_2 \vartheta_{\mathrm{b}}^{\mathrm{e}}) = 0 \quad (2)$$

This equation can be solved numerically for the barrier angle $\vartheta_{\mathrm{b}}^{\mathrm{e}}$. The solutions found are the minima and maxima of the torque ripple.

Fig. 2a reports the torque behaviour due to the first two slot harmonics as a function of the electrical barrier angle, $\vartheta_{\mathrm{b}}^{\mathrm{e}}$. According to a four-pole machine ($2p = 4$), they are the 17th and 19th for the machine with $Q = 36$. These waveforms are obtained through the complete model of the REL machine [6, 26]. This figure shows how much the choice of the flux-barrier angle affects the torque ripple resulting from the harmonic under study. In addition, the vertical lines identify the barrier angles found by the simple formulation derived in (2). It can be noted that the prediction of the torque minima and maxima by (2) perfectly corresponds to the minima computed by means of the complete analytical magnetic model of the machine. As an example, a proper choice of the flux-barrier angle would be ~75° and not 70°.

2.1.2 Two flux-barrier rotor: The equation describing the ripple due to the slot harmonics for a two-flux-barrier motor becomes:

$$\left[\Delta \tau_{\mathrm{m}}^{(h)}\right]^2 \propto \left[\frac{\sin \nu_1 \vartheta_{\mathrm{b}1}^{\mathrm{e}}}{\nu_1} + \frac{\sin \nu_1 \vartheta_{\mathrm{b}2}^{\mathrm{e}}}{\nu_1}\right]^2$$
$$+ \left[\frac{\sin \nu_2 \vartheta_{\mathrm{b}1}^{\mathrm{e}}}{\nu_2} + \frac{\sin \nu_2 \vartheta_{\mathrm{b}2}^{\mathrm{e}}}{\nu_2}\right]^2 \quad (3)$$

In order to get the minima, (3) is derived first by the first barrier angle, $\vartheta_{\mathrm{b}1}^{\mathrm{e}}$, and then by the second one, $\vartheta_{\mathrm{b}2}^{\mathrm{e}}$. This represents a system of two equations in two variables, ($\vartheta_{\mathrm{b}1}^{\mathrm{e}}, \vartheta_{\mathrm{b}2}^{\mathrm{e}}$), and it is solved numerically, both searching for minima and maxima.

Fig. 2b reports the torque behaviours due to the first two slot harmonics in the plane of the two electrical barrier angles $\vartheta_{\mathrm{b}1}^{\mathrm{e}}$ and $\vartheta_{\mathrm{b}2}^{\mathrm{e}}$. These harmonics are of the same order of the previous ones. The two-dimensional maps are again obtained through a complete model of the two flux-barrier REL machine in [26]. Then the points marked by black dots and magenta crosses are found by means of the model proposed in (3). They identify the barrier angles which correspond to the torque ripple minima and maxima, respectively. Once again this model is able to predict these points with satisfactory precision, despite additional assumptions.

2.2 Barriers and islands design

While the choice of the flux-barrier-ends mainly affects the torque ripple, the selection of the magnetic insulation quantity along the q-axis mainly affect the average torque capability of the machine. The thickness of the flux barriers is an important design parameter in order to achieve a good rotor saliency and, therefore, high performance. However, their thicknesses are limited by the level of saturation desired in the rotor iron. This is also the common guideline to choose a proper insulation ratio, k_{air}. In fact, it is often desirable to let the rotor saturate more than the stator teeth, in order to reduce teeth iron losses. The coefficient k_{air} can be computed through the following equation:

$$k_{\mathrm{air}} = 1 - \frac{B_{\mathrm{g}}}{B_{\mathrm{r}}} \cdot \frac{D_{\mathrm{r}}}{p(D_{\mathrm{r}} - D_{\mathrm{sh}})} \quad (4)$$

where B_{g} is the peak air-gap flux density, B_{r} the desired rotor flux density, D_{r} the rotor diameter, D_{sh} the shaft diameter, and p the number of pole pairs. It represents the sum of the barrier thicknesses along the q-axis, that means
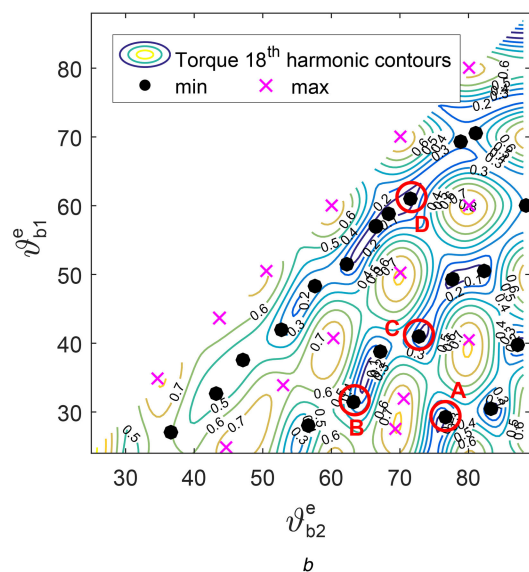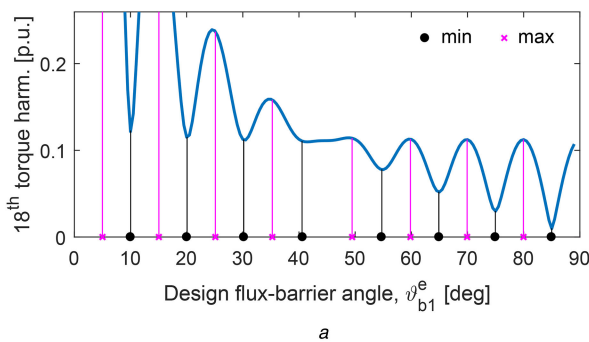

Fig. 2 *Analytical torque maps of the first slot harmonic as a function of the design flux-barrier angles for a 36-slot 4-pole machine. The continuous lines are computed through a complex analytical model while the lines and the markers are obtained with the model described in Section 2.1*
(a) One flux-barrier machine. The vertical lines represent the positions of the torque ripple minima and maxima found by means of (2), *(b)* Analytical torque maps of the first slot harmonic in a two flux-barrier machine. The black dots show the minima found through (3)

$$k_{\text{air}} = \frac{l_{\text{air}}}{l_{\text{tot}}} \quad (5)$$

where $l_{\text{air}} = t_{\text{b1}} + t_{\text{b2}}$ is the amount of magnetic insulation along the q-axis and l_{tot} the available space given by $(D_{\text{r}} - D_{\text{sh}})/2$. Its value typically ranges between 0.4 and 0.6.

2.2.1 Flux-barrier thicknesses: Once the total amount of air is chosen through the coefficient k_{air}, the individual thickness of the flux barriers is chosen according to the stator magnetomotive force (MMF) in front of each barrier: the higher the MMF step between two flux barriers, the thicker the barrier.

Fig. 3a shows a sketch of a two flux-barrier rotor with a sinusoidal q-axis magnetisation. $U_{\text{s}}(\vartheta_{\text{m}})$ and $U_{\text{r}}(\vartheta_{\text{m}})$ represent the stator and the rotor scalar magnetic potentials, respectively. The mean value of $U_{\text{s}}(\vartheta_{\text{m}})$ computed between the flux-barrier end angle $\vartheta_{\text{b}(j-1)}^{\text{e}}$ and $\vartheta_{\text{b}j}^{\text{e}}$ is f_j. For a rotor with two flux barriers, they are:

$$f_1 = \frac{\sin \vartheta_{\text{b1}}^{\text{e}}}{\vartheta_{\text{b1}}^{\text{e}}} \quad \Delta f_1 = f_1 - f_2$$

$$f_2 = \frac{\sin \vartheta_{\text{b2}}^{\text{e}} - \sin \vartheta_{\text{b1}}^{\text{e}}}{\vartheta_{\text{b2}}^{\text{e}} - \vartheta_{\text{b1}}^{\text{e}}} \quad \Delta f_2 = f_2 \quad (6)$$

A common design rule adopted for the flux-barrier thickness ratio is [4]

$$\frac{t_{\text{b2}}}{t_{\text{b1}}} = \frac{\Delta f_2}{\Delta f_1} \sqrt{\frac{\vartheta_{\text{b2}}^{\text{e}}}{\vartheta_{\text{b1}}^{\text{e}}}} \quad (7)$$

and then [27]

$$t_{\text{b1}} = \frac{k_{\text{air}} l_{\text{tot}}}{1 + (\Delta f_2/\Delta f_1)\sqrt{\vartheta_{\text{b2}}^{\text{e}}/\vartheta_{\text{b1}}^{\text{e}}}} \quad (8)$$

so that t_{b2} can be easily obtained through (7). The thickness of each barrier is computed with respect to the q-axis as shown in Fig. 3a.

2.2.2 Iron paths widths: The iron path widths are designed assigning a width proportional to the MMF at the air-gap. Fig. 3b shows a sketch of a two flux-barrier rotor with a sinusoidal d-axis magnetisation. The meaning of f_j is the same of the previous section and the iron paths widths are computed with respect to the q-axis.

The iron path width ratio is defined as

$$\frac{w_{\text{fe},j}}{w_{\text{fe},k}} = \frac{f_j}{f_k}, \quad j,k = 1,2,3 \quad (9)$$

where

$$f_1 = \frac{1 - \cos \vartheta_{\text{b1}}^{\text{e}}}{\vartheta_{\text{b1}}^{\text{e}}}$$

$$f_2 = \frac{\cos \vartheta_{\text{b1}}^{\text{e}} - \cos \vartheta_{\text{b2}}^{\text{e}}}{\vartheta_{\text{b2}}^{\text{e}} - \vartheta_{\text{b1}}^{\text{e}}} \quad (10)$$

$$f_3 = \frac{\cos \vartheta_{\text{b2}}^{\text{e}}}{(\pi/2) - \vartheta_{\text{b2}}^{\text{e}}}$$

Then

$$w_{\text{fe1}} = \frac{(1 - k_{\text{air}})l_{\text{tot}}}{1 + (f_1/f_2) + (f_1/f_3)} \quad (11)$$

and the remaining iron path widths can be determined from (9).

2.3 Iron ribs computation

The thickness of the tangential iron bridges near the air-gap are set equal to the minimum manufacturing length or to the lamination width. Their effect on the structural integrity is negligible.

The radial iron ribs, in the middle of the flux barriers, are properly designed at the rated speed of the motor with the aim of containing the centrifugal stress due to the rotation. A simple analytical method to design the radial rib of each flux-barrier has been described in [25]. Once the flux-barrier end angles are known, it is possible to compute the thickness of the jth flux-barrier as follows:

$$t_{\text{rib }j} = \frac{\nu_\sigma(1 - k_{\text{air}})\gamma_{\text{Lam}}\omega_{\text{m}}^2 D_{\text{r}}^3(2\vartheta_{\text{b}j} - \sin 2\vartheta_{\text{b}j})\cos \vartheta_{\text{b}j}}{8\sigma_{\text{r}}} \quad (12)$$

where ν_σ is a safety factor, γ_{Lam} the lamination mass density, D_{r} the rotor diameter, ω_{m} the mechanical rotor speed, and σ_{r} the tensile strength of the lamination. ω_{m} is often selected slightly higher than the nominal one and ν_σ is set in the range between 2 and 3 [24].

3 Optimisation

For synchronous REL machines, an optimisation of the rotor parameters is almost always necessary to obtain a good design. This statement is reinforced when dealing with high-speed synchronous REL machines. In fact, the presence of iron ribs along the q-axis greatly affects the performance of the machine.

One of the most used optimisation algorithms in electromagnetic designs is differential evolution (DE). Typically, it guarantees good performance and convergence in a reasonable amount of time. Thus, the optimisation procedure used in the following implements a multi-objective DE algorithm.
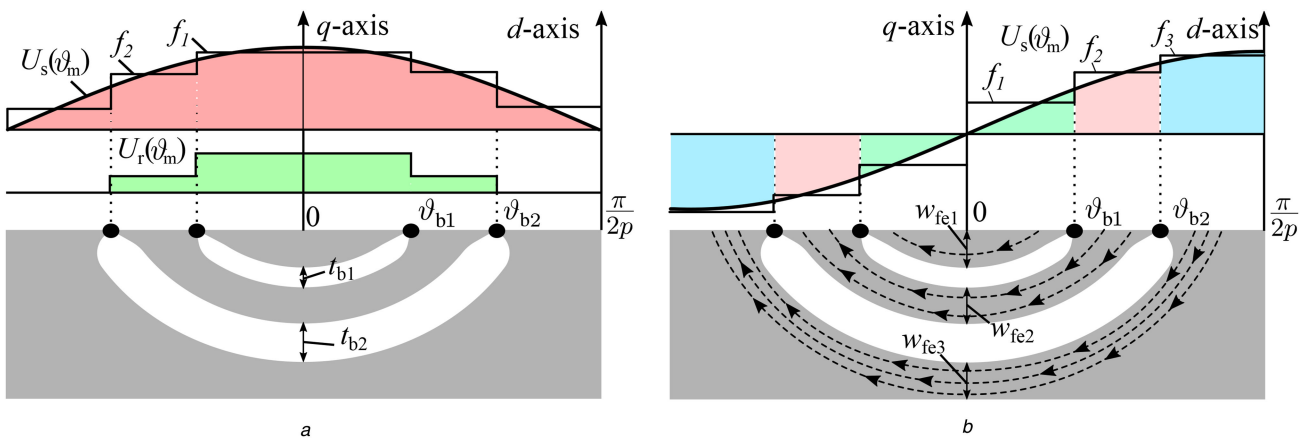

Fig. 3 *Sketches of a two flux barriers per pole rotor with different stator magnetisation*
(a) q-axis magnetisation. The barrier thicknesses are also indicated, *(b)* d-axis magnetisation. The iron path widths are also indicated
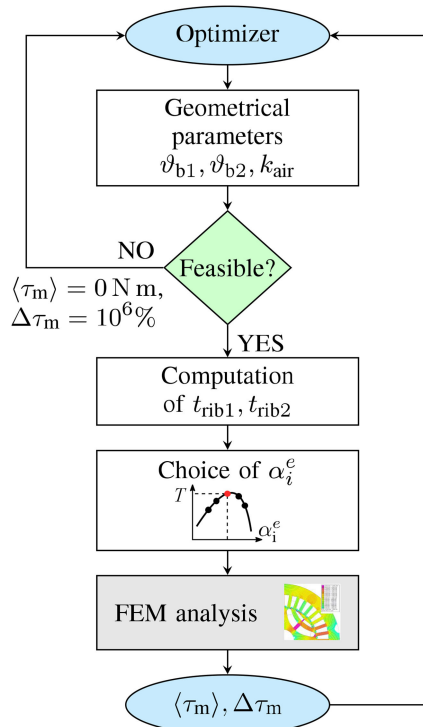
Fig. 4 *Flowchart of the objectives evaluation of the optimiser*

Typical objectives for high-speed machines include the maximisation of average torque (or power), of the saliency, of the power factor, the minimisation of the torque ripple, of the losses or of the cost. The solutions found should also exhibit a proper robustness against slight variations of the design parameters. It is evident that the optimisation of such machines is multi-objective from the start. Therefore, there will not be a single optimum, but many optimal solutions which are called Pareto solutions. In fact, they have at least one of their objectives which is the best among all the solutions.

Fig. 4 shows the flowchart of the evaluation procedure performed for each individual. The geometrical feasibility is evaluated considering the optimiser input parameters. The unfeasible individuals are discarded setting zero average torque and a high torque ripple. For the feasible individuals, the algorithm computes the radial rib thicknesses, finds the maximum torque per Ampere (MTPA) point, and evaluates the average torque, its oscillation, and the motor losses in a sixth of electrical period.

4 Design example

An example of a high-speed synchronous REL motor design is presented hereafter. Two different design methods are proposed: a semi-analytical design approach (SADA) and FE-based optimisation (FEO). In the former, the analytical method is used to select the proper flux-barrier angles combination and to compute the radial rib thicknesses while the FE analysis is used to determine the best insulation ratio and the motor outputs (i.e. average torque, inductances) [28]. The latter needs and optimisation algorithm and FE simulations only. The SADA procedure is faster since it does not require an optimisation. However, the iron saturation is not considered in the flux-barrier angle choice. On the contrary, the total FE procedure requires a higher time consumption (optimiser algorithm), but it is more accurate since it takes into account the iron saturation.

The design only deals with the rotor geometry. The stator, the winding, and the materials are given and reported in Table 1. Through (12), it is possible to estimate if a design for such speed is feasible. In particular, an estimation of the required maximum rib thickness can be made based on the desired design speed. It is sufficient to select ϑ_b equal to the maximum allowable one, which is $\pi/(2p)$. Then, the rib thickness will be a fraction of the

Table 1 Main motor data

Motor output			
rated voltage (RMS)	V_N	400	V
number of poles	$2p$	4	—
mechanical speed	n	30,000	rpm

Geometrical data			
outer diameter	D_e	152	mm
inner diameter	D_i	90	mm
stack length	L_{stk}	100	mm
number of poles	$2p$	4	—
number of slots	Q	36	—
slot height	h_s	16.3	mm
tooth width	w_t	4.14	mm
mechanical air-gap	g	0.7	mm

Winding			
conductors in slot	n_c	6	—
number of parallel paths	n_{pp}	2	—
coil pitch	y_q	8	—

Materials	
iron lamination	N020

Table 2 Flux-barrier end angles combinations that exhibit the lowest torque ripple found through Fig. 2*b*

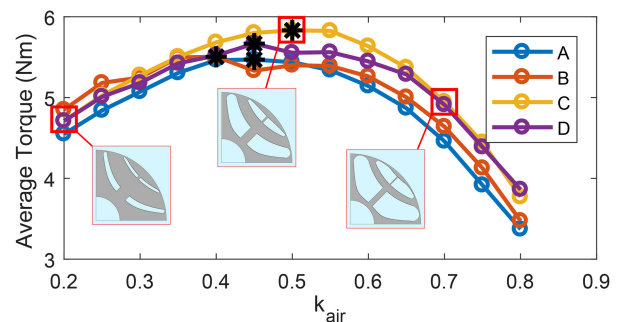| Rotor	ϑ_{b1}^e, deg	ϑ_{b2}^e, deg	ϑ_{b1}, deg	ϑ_{b2}, deg
a	29.25	76.63	14.63	38.32
b	31.49	63.25	15.75	31.63
c	40.96	72.73	20.48	36.37
d	61.02	71.61	30.51	35.81

Fig. 5 *Average torque versus magnetic insulation for different flux-barrier angles*

maximum space available, which means $t_{rib} = c D_r \sin \vartheta_b$, where c measures the fraction. So

$$c = \frac{\nu_\sigma (1 - k_{air}) \gamma_{Lam} \omega_m^2 D_r^2 ((\pi/p) - \sin(\pi/p))}{8 \sigma_r \tan(\pi/2p)} \quad (13)$$

In the present case, considering $k_{air} = 0.5$, $\sigma_r = 500\,\mathrm{MPa}$, $\nu_\sigma = 2.5$, $\gamma_{Lam} = 7650\,\mathrm{kg/m^3}$, it results $c = 0.1$.

4.1 Analytical design

Table 3 Main results obtained through FE analysis of the machines designed with SADA and FEO

Design method	α_i^e, deg	$\langle\tau_m\rangle$, N m	$\Delta\tau_m$, %	L_d, mH	L_q, mH	ξ	$\cos\varphi$
SADA	52.5	5.83	17.6	0.896	0.344	2.61	0.43
FEO	47.5	5.91	9.16	0.910	0.367	2.48	0.40

In Table 2, some flux-barrier angle combinations, which exhibit the lowest torque ripple, are reported. They are selected from the map in Fig. 2b.

The magnetic insulation ratio, k_{air}, can be selected through (4), which gives a value around 0.55 for this machine. However, in this case, the optimal k_{air} has been selected by means of a parametric FE analysis for each considered solution. The results are shown in Fig. 5. The figure also shows the rotor geometry variations with the insulation ratio. It is evident that k_{air} strongly affects the flux-barrier shape and the radial rib thicknesses. In fact, as the coefficient increases, the amount of rotor iron is lower and so, the radial ribs become thinner.

It can be noted that the maximum average torque is achieved with a k_{air} between 0.4 and 0.55. The motor C exhibits the highest average torque among the selected ones. The main motor outputs are reported in Table 3.
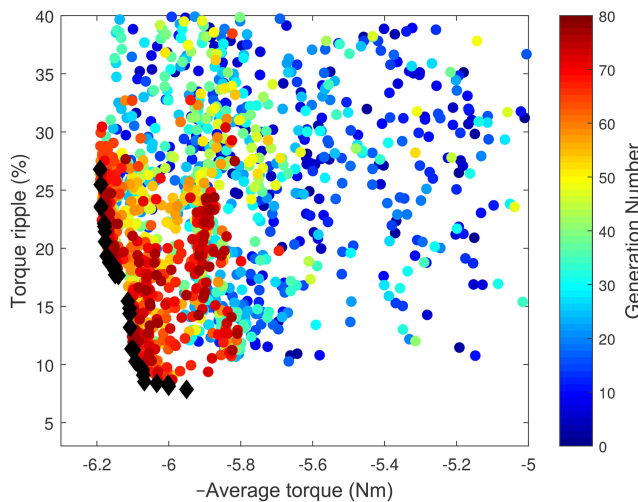

Fig. 6 *Simulated individuals in the objectives plane and Pareto front (black diamonds) at 30,000 rpm*

4.2 FE optimisation

The FE optimisation is carried out with an RMS current density equal to 5.6 A/mm². The selection of the current density is based on an a priori thermal analysis of the machine.

In this case, the chosen objectives are the average torque, $\langle\tau_m\rangle$, and the torque ripple, $\Delta\tau_m$. The geometrical parameters are the two barrier angles, ϑ_{b1}, ϑ_{b2}, and the magnetic insulation ratio, k_{air}, while the other geometrical quantities are derived from these parameters [27].

The optimisation has been carried out with a population size of 25 individuals and 80 generations and it took ~2 days. The final objectives plane is shown in Fig. 6. The black diamonds represent the Pareto front. For high-speed applications, it is mandatory to limit the torque oscillation that causes dangerous mechanical vibrations and acoustic noise. For this reason, the individual with the lowest torque ripple has been selected. The average torque is ~6 N m, while the torque ripple is ~9% with respect to the average torque. The related barrier angles are $\vartheta_{b1} = 20.70°$ and $\vartheta_{b2} = 31.81°$, while the insulation ratio is 0.429. With respect to the flux-barrier end angles analytically predicted, the first one is practically the same, while the second one is 9.12° (electrical) lower. The different rotor configurations justify the mismatch of the torque ripple obtained with the two methods.

4.3 Electromagnetic analysis

After the selection of the most promising solution, an in-depth electromagnetic analysis is required to precisely evaluate the machine performances. In particular, the average torque and the torque ripple found through the optimisation are confirmed and better estimated, as reported in Fig. 7a. The numerical results are also reported in Table 3.

The flux density plot of the FE optimal motor is shown in Fig. 8a. It can be noted that the iron saturation within the tangential ribs covers a larger area and the iron saturation of channels is not negligible. These aspects highly affect the analytical model hypothesis and explain the different torque ripple predicted by the approaches.
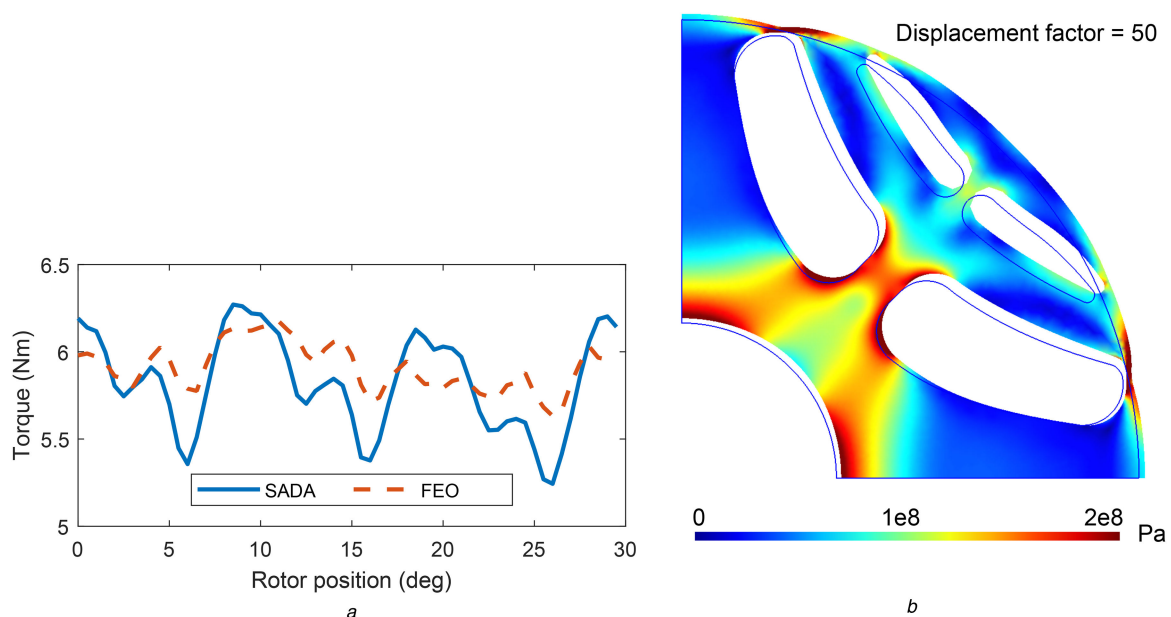

Fig. 7 *Plots resulting from the FE analysis*
(a) FE torque versus rotor position with different flux-barrier angles, *(b)* Von Mises stress of the optimised rotor for 30,000 rpm
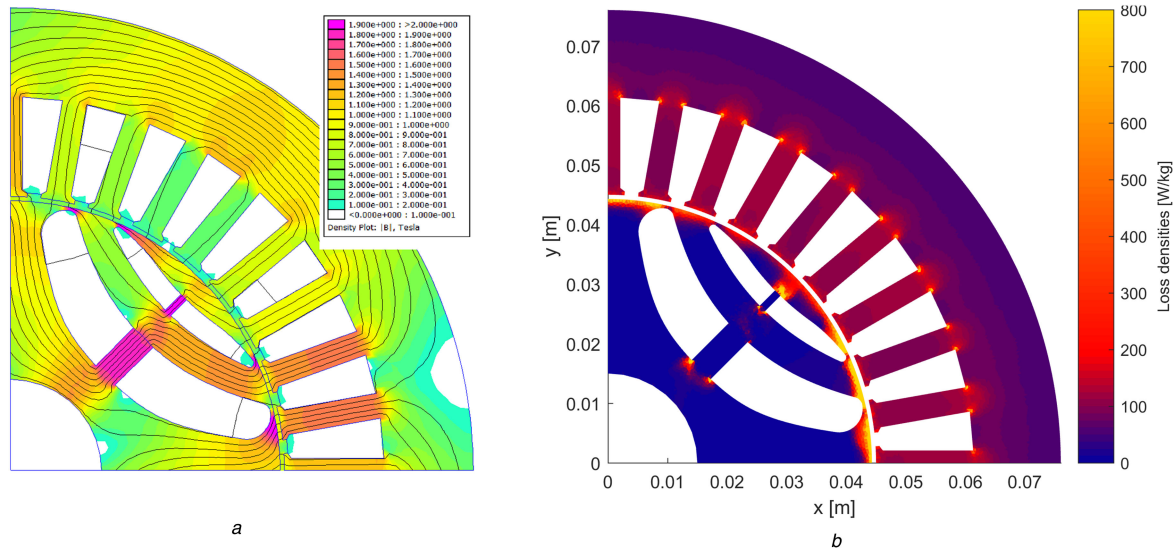
Fig. 8 *Plots of the rotor designed with the FE approach*
(a) Flux density plot, *(b)* Loss density map at the MTPA operating point

Table 4 Motor losses in different parts

Part	Losses, W		
	Fundamental	Space harmonics	Total
copper	194	0	194
stator iron	479	100	579
rotor iron	0	159	159
total	673	259	932

The high speed of rotation involves high frequency for the current supply. Even though thin lamination sheets have been considered, iron losses may play an important role in the overall machine performance. So, to accurately estimate the losses, the flux density for every mesh element has been recorded in both *x* and *y* directions for a complete electrical rotation. This allows us to split the flux density fluctuations in Fourier series and, thus, to find the losses for all the harmonics involved. The harmonic losses are caused by the staircase MMF waveform and by the effect of stator slots. Current distortion may introduce additional losses, but it is not considered in this study.

The loss density map is reported Fig. 8*b*. It can be noted that the maximum loss density appears near the rotor periphery and near sharp corners. However, the volumes involved are rather small. On the other hand, stator teeth and back-iron see lower loss densities but they are diffused, filling almost the entire volume. In fact, the stator iron is subjected also to the fundamental harmonic of the flux density, which is obviously the highest harmonic.

The numerical comparison among the losses is reported in Table 4. The majority of losses is due to the iron losses in the stator caused by the fundamental of the flux density. Joule losses in the stator winding are the second main cause. Then it can also be seen that the additional losses introduced by the harmonics are not negligible at this speed, as they represent almost 30% of the total electromagnetic losses.

5 Structural analysis

Lastly, a structural FE analysis has to be performed to verify whether the radial iron ribs are able to sustain the centrifugal load of the rotor iron paths [29, 30]. In the present study, only the rotor design with the FE optimisations is considered since it achieves better performance. Furthermore, the two rotor geometry are similar from the mechanical point of view.

The rotor sharp corners have been smoothed out in order to avoid dangerous stress concentrations. The von Mises stress and the displacement plots are shown in Fig. 7*b*. The ultimate tensile strength of the selected material is 500 MPa, while the chosen safety factor is 2.5 [24]. The scale of the von Mises stress has been

set to the desired stress value, which is 200 MPa for this study. It can be observed that the target stress value is never reached within the radial iron ribs. Stress concentration is present near corners, but it will lead only to some yielding.

6 Conclusion

The aim of this present paper is to propose a procedure to design synchronous REL motors for high-speed applications. Only the rotor geometry has been properly designed while the stator and the winding have been kept fixed. The goals of the rotor design are to achieve the maximum torque density with the lowest torque ripple and to ensure the structural integrity against the high centrifugal force. To do that, the flux-barrier geometries (i.e. angles, thicknesses) and the radial ribs have been designed. Two design approaches have been proposed: one is semi-analytical, while the other is based on FE optimisation. The former is faster and finds suitable flux-barrier angles by means of a simple analytical model. The motor performance is then precisely evaluated through FE analysis. The latter is more accurate since it considers the iron saturation but requires more time because of the optimisation algorithm. The comparison between the two methods revealed that the non-localised saturation of the tangential ribs and the radial rib thicknesses strongly affect the torque ripple estimation of the analytical model. For this reason, the torque oscillation obtained by means of the FE optimisation is ∼52% of that resulting from the semi-analytical approach.

The losses computation has shown that rotor losses have to be taken into account for an accurate efficiency prediction, especially at such high speeds. In fact, the rotor losses represent ∼30% of the total. The structural analysis confirmed the validity of the radial ribs design method giving a suitable stress distribution within the rotor.

In conclusion, the semi-analytical method is a quick procedure that allows to obtain a good initial design of a synchronous REL rotor. However, to get more performing designs, a multi-objective optimisation algorithm should be employed.

7 References

[1] Moghaddam, R., Magnussen, F., Sadarangani, C.: 'Novel rotor design optimization of synchronous reluctance machine for high torque density'. 6th IET Int. Conf. on Power Electronics, Machines and Drives (PEMD 2012), Bristol, UK, 2012, pp. B32–B32. Available at http://digital-library.theiet.org/content/conferences/10.1049/cp.2012.0256

[2] Barcaro, M., Bianchi, N.: 'Interior PM machines using ferrite to replace rare-earth surface PM machines', *IEEE Trans. Ind. Appl.*, 2014, **50**, (2), pp. 979–985

[3] Fratta, A., Villata, F., Vagati, A.: 'Permanent magnet assisted synchronous reluctance drive for constant-power application: drive power limit'. Intelligent Motion European Conf., PCIM, Nurnberg, Germany, 1992, pp. 196–203

[4] Vagati, A., Pastorelli, M., Franceschini, G.*, et al.*: 'Design of low-torque-ripple synchronous reluctance motors', *IEEE Trans. Ind. Appl.*, 1998, **34**, (4), pp. 758–765

[5] Miller, T.J.E., Hutton, A., Cossar, C.*, et al.*: 'Design of a synchronous reluctance motor drive', *IEEE Trans. Ind. Appl.*, 1991, **27**, (4), pp. 741–749

[6] Barcaro, M.: 'Design and analysis of interior permanent magnet synchronous machines for electric vehicles'. PhD thesis, University of Padova, 2011

[7] Taghavi, S., Pillay, P.: 'Design aspects of a 50 hp 6-pole synchronous reluctance motor for electrified powertrain'. IECON 2017, Beijing, China, 2017

[8] Bianchi, N., Bolognani, S., Pr, M.D.: 'Design of a fault-tolerant IPM motor for electric power steering', *IEEE Trans. Veh. Technol.*, 2006, **55**, (4), pp. 2873–2880

[9] Welchko, B.A., Jahns, T.M., Soong, W.L.*, et al.*: 'IPM synchronous machine drive response to symmetrical and asymmetrical short circuit faults', *IEEE Trans. Energy Convers.*, 2003, **18**, (2), pp. 291–298

[10] Staton, D., Miller, T., Wood, S.: 'Maximising the saliency ratio of the synchronous reluctance motor', *IET Electr. Power Appl.*, 1993, **140**, (4), pp. 249–259

[11] Lipo, T.A., Vagati, A., Miller, T.*, et al.*: '*Synchronous reluctance motors and drives – a new alternative*' (IEEE Industry Applications Society, Denver, 1994)

[12] Moghaddam, R.R., Gyllensten, F.: 'Novel high-performance SynRM design method: an easy approach for a complicated rotor topology', *IEEE Trans. Ind. Electron.*, 2014, **61**, (9), pp. 5058–5065

[13] Moghaddam, R.R., Magnussen, F., Sadarangani, C.: 'Theoretical and experimental reevaluation of synchronous reluctance machine', *IEEE Trans. Ind. Electron.*, 2010, **57**, (1), pp. 6–13

[14] Pellegrino, G., Cupertino, F., Gerada, C.: 'Barriers shapes and minimum set of rotor parameters in the automated design of synchronous reluctance machines'. 2013 Int. Electric Machines Drives Conf., Chicago (Rosemont), Illinois, USA, 2013, pp. 1204–1210

[15] Fratta, A., Troglia, G., Vagati, A.*, et al.*: 'Evaluation of torque ripple in high performance synchronous reluctance machines'. Record of the IEEE Industry Applications Society Annual Meeting, Toronto, ON, Canada, 1993, pp. 163–170

[16] Jahns, T.M., Soong, W.L.: 'Pulsating torque minimization techniques for permanent magnet AC motor drives – a review', *IEEE Trans. Ind. Electron.*, 1996, **43**, (2), pp. 321–330

[17] Bianchi, N., Bolognani, S., Bon, D.*, et al.*: 'Torque harmonic compensation in a synchronous reluctance motor', *IEEE Trans. Energy Convers.*, 2008, **23**, (2), pp. 466–473

[18] Bacco, G., Bianchi, N.: 'Choice of flux-barriers position in synchronous reluctance machines'. 2017 IEEE Energy Conversion Congress and Exposition (ECCE), Cincinnati, 2017, pp. 1872–1879

[19] Ikäheimo, J., Kolehmainen, J., Känsäkangas, T.*, et al.*: 'Synchronous high-speed reluctance machine with novel rotor construction', *IEEE Trans. Ind. Electron.*, 2014, **61**, (6), pp. 2969–2975

[20] Boules, N.: 'Impact of slot harmonics on losses of high-speed permanent magnet machines with a magnet retaining ring', *Electr. Mach. Power Syst.*, 1981, **6**, (6), pp. 527–539

[21] Zhu, Z.Q., Ng, K., Howey, D.A.: 'Design and analysis of high-speed brushless permanent magnet motors'. Proc. of Electrical Machines and Drives (EMD) Conf., Cambridge, UK, 1997, pp. 381–385

[22] Castagnini, A., Garavaglia, M., Moriconi, F.*, et al.*: 'Development of a very high speed and power synchronous PM motor'. Proc. of Int. Conf. Electrical Machine (ICEM), Brugges, Belgium, 2002, pp. 25–28

[23] Bianchi, N., Bolognani, S., Luise, F.: 'Potentials and limits of high-speed PM motors', *IEEE Trans. Ind. Appl.*, 2004, **40**, (6), pp. 1570–1578

[24] Barcaro, M., Meneghetti, G., Bianchi, N.: 'Structural analysis of the interior PM rotor considering both static and fatigue loading', *IEEE Trans. Ind. Appl.*, 2014, **50**, (1), pp. 253–260

[25] Babetto, C., Bacco, G., Bianchi, N.: 'Analytical approach to determine the power limit of high-speed synchronous reluctance machines'. 2017 IEEE Int. Electric Machines and Drives Conf. (IEMDC), Miami, 2017, pp. 1–7

[26] Bianchi, N., Bolognani, S., Bon, D.*, et al.*: 'Rotor flux-barrier design for torque ripple reduction in synchronous reluctance and PM-assisted synchronous reluctance motors', *IEEE Trans. Ind. Appl.*, 2009, **45**, (3), pp. 921–928

[27] Wang, Y., Bacco, G., Bianchi, N.: 'Geometry analysis and optimization of PM-assisted reluctance motors', *IEEE Trans. Ind. Appl.*, 2017, **53**, (5), pp. 4338–4347

[28] Meeker, D.: 'Finite element method magnetics', 2009. Available at http://www.femm.info/Archives/doc/manual.pdf

[29] Dular, P., Geuzaine, C.: 'GetDP reference manual: the documentation for GetDP, a general environment for the treatment of discrete problems'

[30] Dular, P., Geuzaine, C., Henrotte, F.*, et al.*: 'A general environment for the treatment of discrete problems and its application to the finite element method', *IEEE Trans. Magn.*, 1998, **34**, (5), pp. 3395–3398

1116

IET Electr. Power Appl., 2018, Vol. 12 Iss. 8, pp. 1110-1116